Quantum Electronics **52** (5) 482–490 (2022)

LASER BIOPHOTONICS https://doi.org/10.1070/QEL18047

Assessment of the thermal effect of femtosecond and millisecond laser pulses in microsurgery of mammalian embryos

D.S. Sitnikov, I.V. Ilina, A.A. Pronkin

Abstract. **We compare the thermal effect exerted by femtosecond and millisecond pulses during microsurgical procedures on embryos. The linear and nonlinear absorption of laser pulses in an aqueous medium, as well as heat transfer from the focusing region of the laser beam to adjacent regions, are considered.**

Keywords: *femtosecond pulses, multiphoton absorption, avalanche ionisation, aqueous medium, millisecond pulses, dissector, thermal effect, embryo.*

1. Introduction

Modern sources of ultrashort laser radiation pulses (hereafter, we mean a duration $\tau_L < 10$ ps) are widely used in applications based on laser-induced plasma formation processes, including photomodification of biomolecules [1, 2] and in laser surgery [3–5]. The advent of femtosecond lasers opened up new possibilities in the field of refractive keratoplasty [4, 6] and contributed to the development of Femto-LASIK technology, which made it possible to eliminate the use of mechanical instruments. However, in the field of assisted reproductive technologies (ARTs), ultrashort duration radiation sources have not yet received the recognition they deserve. Currently, millisecond laser dissectors are widely used for embryonic microsurgery (mainly for affecting the transparent membrane of the embryo, referred to as the *zona pellucida*) [7]. The arsenal of commercially available systems includes the ZILOS-tk® (Hamilton Thorne), Saturn 5™ (CooperSurgical®) and OCTAX Laser Shot™ (MTG) models. They differ in degrees of automation and gradually replace mechanical instruments and chemical techniques in clinical practice. At the same time, their use has certain risks associated with thermal damage to the embryo cells, closely adjacent to the *zona pellucida* of the embryo from the inside. In studies [7, 8] devoted to the search for safe regimes of laser exposure, it was shown that the temperature at the centre of the beam reaches several hundred degrees and remains at a level of ~100 °C even at a distance of 10 μm. Thus, when using millisecond dissectors for embryonic microsurgery, it is necessary to comply with a number of strict safety requirements to eliminate the risk of damage to embryonic cells [9].

D.S. Sitnikov, I.V. Ilina, A.A. Pronkin Joint Institute for High Temperatures, Russian Academy of Sciences, ul. Izhorskaya 13, stroenie 2, 125412 Moscow, Russia; e-mail: Sitnik.ds@gmail.com

Received 29 November 2021; revision received 20 March 2022
Kvantovaya Elektronika **52** (5) 482–490 (2022)
Translated by V.L. Derbov

Femtosecond laser dissectors are a promising alternative to millisecond ones, since the nonlinear mechanisms of absorption of femtosecond laser radiation in an aqueous medium make it possible to localise the interaction area, significantly increasing the accuracy of microsurgical procedures. This, in turn, will improve the safety of laser microsurgery of embryos and expand the scope of lasers in demanded ART tasks. For example, the technology of noncontact laser marking of preimplantation embryos was recently implemented based on a femtosecond laser dissector to identify them and eliminate the risk of mix-up [10], as well as the technology of controlled laser hatching at the late stages of preimplantation development [11].

A large number of studies have been devoted to the description of the interaction of femtosecond laser pulses with dielectric media, including the formation of an electron–hole plasma, optical breakdown, and shock waves (see, e.g., [12–17]). However, the assessment of the thermal impact of femtosecond laser pulses with parameters corresponding to those optimal for performing embryo microsurgical procedures has not been previously carried out. In the present work, we obtained data on the spatial and temporal distributions of temperature in the area affected by a femtosecond laser pulse and compared it with the result of exposure to a millisecond pulse. For this purpose, we used a model previously developed and described in detail by a group of authors in a series of papers of 2003–2019 [18–21]. The model serves to calculate the energy density of laser-induced electrons in the focusing region, which determines the spatiotemporal profile of a heat source when solving the heat transfer problem.

2. Modelling the interaction process

2.1. Ionisation of water

In 1986, it was experimentally shown [22] that the breakdown thresholds in water and in biological tissues are very close, which subsequently led to the use of water parameters in modelling the processes of ultrashort pulse (USP) action on biological tissues. Williams et al. [23] proposed to consider water as an amorphous semiconductor. Water spectroscopy data obtained over the past two decades have allowed the concept of its band structure to be refined. According to modern concepts, a direct transition of an electron from the valence band (VB) to the conduction band (CB) (ionisation) is possible at electron energies of at least 9.5 eV [24, 25]. What previously was considered as an ionisation energy of 6.5 eV is the minimum energy required for direct excitation of an electron from the VB to the solvated state [26]. In this case, ioni-

sation can be considered as a two-stage process, including the creation of solvated electrons e^-_{aq} with their subsequent transition to the CB (Fig. 1). This intermediate energy level, located 6.6 eV above the upper boundary of the VB, has a final capacity $\chi_{trap} \approx 10^{19}$ cm^{-3}, which is approximately three traps per 1000 water molecules [27]. The solvated electrons e^-_{aq} can easily be transferred to the CB because the energy difference is only 3 eV. In the case of IR laser pulses, the process occurs either due to multiphoton absorption or stepwise, through intermediate p states [28].

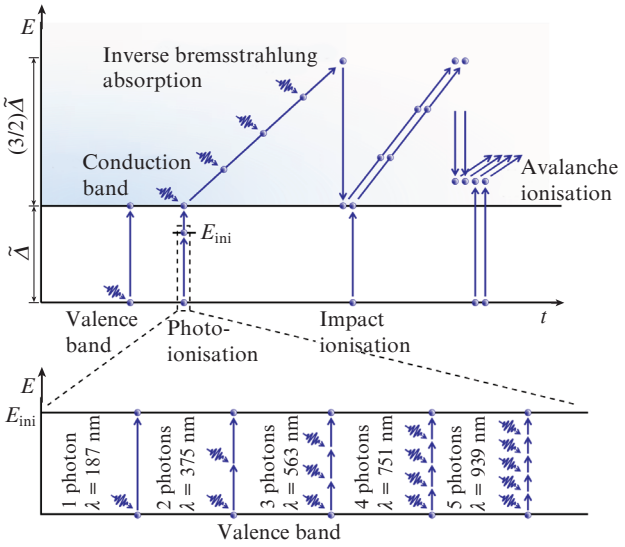

Figure 1. (Colour online) Schematic of water ionisation under the influence of laser radiation pulses.

Thus, the excitation of an electron with its transition from the VB to the CB occurs through strong field ionisation (SFI) and can occur both directly and through an intermediate level with the energy E_{ini} (called 'initiation channel' in Refs [20, 27]). Hereafter, we will adhere to the same terminology. The SFI rate is determined by the expression

$$\frac{d\rho_{SFI}}{dt} = \frac{d\rho_{ini}}{dt} + \frac{d\rho_{E_{gap}}}{dt}, \quad (1)$$

where

$$\frac{d\rho_{E_{gap}}}{dt} = \eta_{SFI}(\tilde{\Delta}); \quad (2)$$

$$\frac{d\rho_{ini}}{dt} = \eta_{SFI}(E_{ini})\left(1 - \frac{\rho_{ini}}{\rho_{ini}^{max}}\right); \quad (3)$$

ρ_{ini}, $\rho_{E_{gap}}$, and ρ_{SFI} are the electron concentrations achieved in CB through the initiation channel or by direct excitation from the VB to the CB across the bandgap E_{gap}, and the total value obtained as a result of SFI (i.e., without taking into account avalanche ionisation), respectively; and ρ_{ini}^{max} is the maximum concentration value for the initiation channel, which is assumed in Ref. [20] to be $\sim 10^{19}$ cm^{-3}. The function $\eta_{SFI}(\ldots)$ is a set of Keldysh expressions [19, 29]. The total energy required for the transition of an electron from the VB to the CB is determined by the ionisation potential $\tilde{\Delta}$, which takes into account both the width of the band gap itself and the energy of vibrations of free electrons in strong electromagnetic fields [20, 29]:

$$\tilde{\Delta} = \frac{2}{\pi} E_{gap} \frac{\sqrt{1+\gamma^2}}{\gamma} E\left(\frac{1}{\sqrt{1+\gamma^2}}\right), \quad (4)$$

where

$$\gamma = \frac{\omega}{e}\sqrt{\frac{m' c n_0 \varepsilon_0 E_{gap}}{I}}$$

is the Keldysh parameter that determines the SFI regime: tunnelling at $\gamma \ll 1$ and multiphoton at $\gamma \gg 1$; ω is the circular frequency of the laser pulse electric field; e is the electron charge; n_0 is the refractive index of the medium at frequency ω; c is the speed of light in vacuum; ε_0 is the permittivity; I is the intensity of the laser pulse; m' is the reduced exciton mass (taken equal to half the electron mass) [30, 31]; and the function $E(\ldots)$ is an elliptic integral of the second kind.

It can be seen from Fig. 1 that UV radiation requires a significantly smaller number of photons involved in the ionisation process than radiation in the visible or IR range. As a result, at the same intensity for the UV laser pulse, the process of multiphoton absorption at the front of the laser pulse 'turns on' earlier than for visible and IR radiation. Taking into account these differences, an approximation was proposed in [27] that provides good agreement between the threshold of water breakdown intensities $I_{th}(\lambda)$ for nanosecond laser pulses, which was subsequently used in [20] for femtosecond pulses:

$$E_{ini}(\lambda) = \begin{cases} -(27/22400)\lambda + 7.59 \text{ for } \lambda \leqslant 990 \text{ nm}, \\ 6.4 \text{ for } \lambda > 990 \text{ nm}, \end{cases} \quad (5)$$

where the energy E_{ini} is expressed in eV. To estimate the electron concentration achieved through the initiation channel, Eqn (5) was substituted into Eqn (3).

Electrons in the CB, having received through inverse Bremsstrahlung absorption (IBA) the energy E_{crit} sufficient for impact ionisation, contribute to the further generation of free electrons. To fulfil the laws of energy and momentum conservation, the energy of the incident electron must be greater than the effective ionisation potential $\tilde{\Delta}$. For a parabolic band gap, the minimum energy is $E_{crit} = (3/2)\tilde{\Delta}$ [13, 19, 32]. The distribution of excess electron energy remaining after impact ionisation is considered in detail in Ref. [21].

To track the dynamics of the electron energy distribution in the CB during femtosecond breakdown, it was proposed in 2004 to use a multi-rate equation (MRE) [13], which allows the contributions of SFI and avalanche ionisation (AI) to be taken into account. Within the framework of this approach, a set of energy levels in the CB is introduced and the population dynamics at each of them is monitored. For long pulses (the criterion concerning the pulse duration is given below), an asymptotic solution was found in which avalanche ionisation was described by a single-rate equation (SRE), which does not allow information about the energy spectrum and volume energy density in the dielectric to be obtained. The solution to the problem was proposed [31] in the form of taking into account the distributions of the residual energy after impact ionisation over energy levels, introduced in the classical model described by the MRE. However, this approach turned out to be extremely resource-intensive and demanding on the com-

puting power. Therefore, in [21], the limits of applicability of all three mentioned models were estimated from the point of view of the laser radiation intensity and wavelength. The use of the SRE is acceptable under the following conditions:

$$\tau_L \gg t_{asymp}, \quad \alpha_{imp} \gg W_{1pt}, \tag{6}$$

where τ_L is the laser pulse duration (FWHM); t_{asymp} is the time for the process to reach the stationary regime with a constant ionisation rate; α_{imp} is the ionisation rate taken in [21] to be 10^{15} s^{-1}; and W_{1pt} is the single-photon excitation rate in the Drude model, which is a function of the intensity and carrier frequency of the laser pulse. It was shown that condition (6) is satisfied for a pulse with duration $\tau_L = 250$ fs and intensity $I = 8.3 \times 10^{12}$ W cm^{-2}, which corresponds to the threshold intensity of water breakdown both at the fundamental frequency ($\lambda = 1028$ nm) and at the frequency of the second harmonic ($\lambda = 514$ nm). In this case, the SRE gives slightly overestimated values of the electron density in the CB compared to the MRE, which, however, is easily compensated by an increase in the effective collision time in the Drude model: $\tau_{coll} = 1$ fs for the SRE and $\tau_{coll} = 0.9$ fs for the MRE [20].

In the present work, the asymptotic avalanche ionisation model in combination with the two-channel SFI model was used in calculations, and the general equation for assessing the electron dynamics in the CB was

$$\frac{d\rho_c}{dt} = \frac{d\rho_{SFI}}{dt} + \eta_{AI}^{asymp}\rho_c - \eta_{rec}\rho_c^2, \tag{7}$$

where η_{rec} is the velocity recombination, which is taken equal to 1.8×10^{12} cm^3 s^{-1} in calculations and is the average value of the rates obtained in Refs [33] (2×10^{12} cm^3 s^{-1}) and [34] (1.6×10^{12} cm^3 s^{-1}); and ρ_c is the electron concentration. To estimate the avalanche ionisation rate in the asymptotic approximation, one can use the relation [20]

$$\eta_{AI}^{asymp} \approx \ln 2 \frac{\tau_{coll}}{\omega^2\tau_{coll}^2 + 1}\left[\frac{e^2 I}{cn_0\varepsilon_0 m'(3/2)\tilde{\Delta}}\right], \tag{8}$$

where the laser pulse is approximated by the Gaussian function

$$I(t) = I_0 \exp[-4\ln 2(t/\tau_L)^2], \tag{9}$$

and the peak value of the pulse intensity is

$$I_0 = 2(\ln 2/\pi)^{1/2} F_0/\tau_L. \tag{10}$$

Here F_0 is the energy density of the laser beam. The spatial intensity distribution at the focus of the laser beam, by analogy with Ref. [19], is determined by the expression

$$I(r,z) = I_0 \exp\left[-2\left(\frac{r^2}{a^2} + \frac{z^2}{b^2}\right)\right], \tag{11}$$

where r is the radial coordinate corresponding to the distance from the laser beam axis; a and b are the minor and major axes of the ellipse-shaped focal spot of the laser beam (the cross section has a Gaussian shape, the values are taken at the $1/e^2$ level) with the central intensity $I(0,0) = I_0$. The z axis coincides with the laser beam axis and is directed towards its propagation. The beam waist plane has the coordinate $z = 0$.

2.2. Dynamics of the thermal effect

The thermal effect of a femtosecond pulse was estimated earlier [19, 20], where the temperature increase ΔT in the region of laser radiation focusing was estimated through the electron energy density

$$U = \rho_c(\tilde{\Delta} + \bar{E}_{kin}), \tag{12}$$

where $\bar{E}_{kin}$ is the average the kinetic energy of electrons, which, assuming a uniform distribution of electrons over energy levels in the CB, is equal to $(5/4)\tilde{\Delta}$ [20]. Then, taking into account the density ρ_0 and specific heat capacity C_p of water, the temperature increase can be estimated as

$$\Delta T = \frac{U}{\rho_0 C_p} = \frac{9}{4}\frac{\rho_c\tilde{\Delta}}{\rho_0 C_p}. \tag{13}$$

This approach makes it possible to estimate the maximum temperature in the affected area; however, to study the temperature dynamics, the solution of the heat conduction problem is required.

2.2.1. Modelling area: geometry and boundary conditions. Consider the procedure of laser microsurgery of the embryo in more detail. A typical view of a preimplantation mammalian embryo in the early stages of development is shown in Fig. 2. Similar to an oocyte, a protective glycoprotein shell (*zona pellucida*) surrounds the embryo in the first five to seven days of its development. The most popular embryo microsurgical procedures are precisely the laser effect on the tprotective shell [35]. Laser USPs have been successfully used to dissect the *zona pellucida* and form a hole in it [36] for further taking of cellular material and performing preimplantation genetic diagnosis (the so-called polar body biopsy [37]), as well as for biopsy of trophectoderm cells [38] and fusion of blastomeres [39, 40]. The impact of femtosecond laser pulses with the aim of partial or complete disruption of the integrity of the *zona pellucida* at various stages of preimplantation development of embryos to stimulate their hatching from the shell and

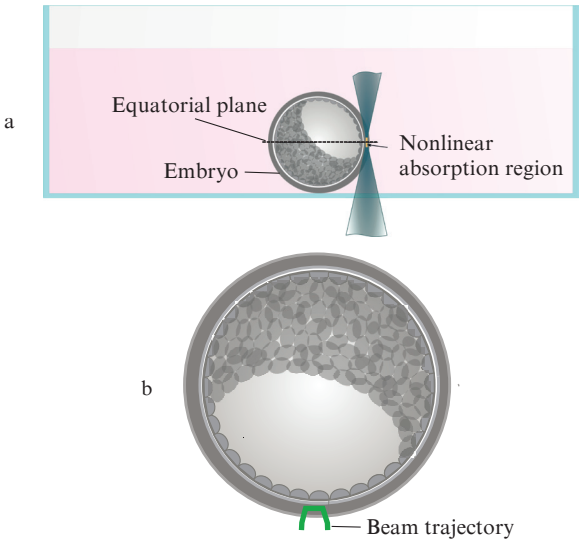

Figure 2. (Colour online) Explanations for the procedure of embryo microsurgery with femtosecond laser pulses: (a) side view and (b) the trajectory of the beam in the equatorial plane.

increase the chances of successful implantation in the uterine cavity has also been demonstrated in recent publications [11, 41]. Using femtosecond laser pulses, it became possible to develop a technology that involves applying a unique alphanumeric code to the protective shell of embryos to identify embryos at all stages of preimplantation development and eliminate the risk of their 'mix-ip' [42, 43].

Briefly, the procedure for laser microsurgery of the shell of embryos using femtosecond laser pulses is performed as follows. Embryos obtained according to precise protocols [44] are cultivated to the required developmental stage in an incubator under optimal conditions (37 °C, 5% CO_2). Before carrying out microsurgical procedures, they are removed from the incubator and transferred to a specialised environment for manipulations in a Petri dish with a glass bottom. Then the Petri dish is fixed on the motorised object stage of the inverted microscope, which is part of the femtosecond scalpel-optical tweezers setup [45]. Next, the operator finds the selected embryo in the cup, marks the beam trajectory in specialised software, and launches an automated laser exposure procedure. Microsurgical impact is implemented by a sequence of laser pulses while moving the object relative to the fixed beam. The duration of the procedure is a few seconds. After that, the operator removes the Petri dish into the incubator. Since the total time the dish is outside the incubator does not exceed 5 min, the initial temperature T_0 of the medium (water) in the simulation is taken to be 37 °C.

We consider the case of laser beam focusing through the glass bottom of a Petri dish in the equatorial plane of the embryo (the plane of the largest section). The latter is located at a distance of ~75 μm above the surface of the cup bottom (Fig. 2). Thus, when modelling the laser action, the medium has the shape of a cylinder with a radius b_c and a height h_c, the axis of which coincides with the axis of the laser beam (Fig. 3). The temperature of the cylinder walls is taken equal to a constant ($T = T_0$), and the boundary conditions correspond to the Dirichlet conditions. The upper surface of the cylinder is the water–air interface, the temperature of which under the lid of the Petri dish is assumed to be constant ($T_0 = 37$ °C).

2.2.2. Heat transfer problem. It should be noted that the problem of assessing the thermal effect of laser pulses on the embryo was considered earlier [7, 8] for pulse durations τ_L = 0.6 and 3 ms at a wavelength of 1480 nm, typical for commercially available laser dissectors in *in vitro* fertilisation (IVF) clinics. Comparison of the results of solving the problem for millisecond and femtosecond pulses is of interest from the point of view of assessing the thermal effect exerted on the embryo. Therefore, we simulated the impact of a femtosecond pulse using the geometry of the problem solved earlier [7, 8].

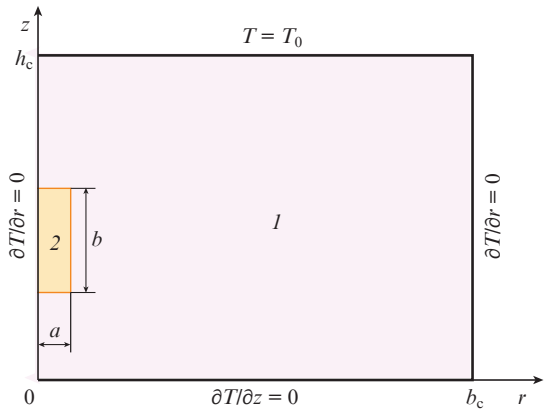

Figure 3. (Colour online) Boundary conditions for the heat transfer problem: (*1*) medium at temperature $T = T_0$; (*2*) region of laser beam waist.

The heat conduction equation in cylindrical coordinates can be written in the form

$$\rho_0 C_p \frac{\partial T}{\partial t} = k(T)\left[\frac{1}{r}\frac{\partial}{\partial r}\left(\frac{r\partial T}{\partial r}\right) + \frac{\partial^2 T}{\partial z^2}\right] + S, \tag{14}$$

where the water density ρ_0 is taken in kg m^{-3}, and its specific heat C_p is in J K^{-1} kg^{-1}; and S is the power density of the source. The dependence of the thermal conductivity of water $k(T)$ (in W m^{-1} K^{-1}) on temperature in the range of 0–100 °C was presented earlier in Ref. [46]:

$$k(T) = 0.6065\left(-1.48445 + \frac{4.12292}{298.15}T - \frac{1.63866}{298.15^2}T^2\right). \tag{15}$$

2.2.3. Heat source function. When using millisecond pulses, the linear absorption process plays a key role, since the laser pulse heats up the medium as it propagates. In this case, the heat source function can be represented separately for the waist region with radius $r_0 = a$ [8]:

$$S_0 = \frac{\alpha P}{\pi a^2}\exp\left[-2\left(\frac{r}{a}\right)^2\right], \tag{16}$$

as well as for the convergent and divergent regions of the focused laser beam:

$$S_\pm = \frac{\alpha P}{2\pi(1-\cos\theta)}\frac{1}{r^2+z^2}\exp\left\{-2\left[\frac{\arctan(r/z)}{\theta}\right]^2\right\}$$
$$\times\exp[\pm\alpha(r^2+z^2)^{1/2}], \tag{17}$$

where P is the source power; θ is the cone angle for the convergent and divergent regions of the laser beam; and α is the absorption coefficient, which at the wavelength of the millisecond laser dissector (as in [8]) is taken equal to 21 cm^{-1} [47]. The angle θ is determined by the numerical aperture NA of the focusing microscope objective and the refractive index of the medium: $\theta = \arcsin(\mathrm{NA}/n_0)$.

When exposed to a millisecond pulse, in [7, 8] the time profile of the power density of the heat source had a stepped form and was specified by the condition

$$S = \begin{cases} S_\Sigma, & t \leqslant \tau_L, \\ 0, & t > \tau_L, \end{cases} \tag{18}$$

where $S_\Sigma = S_0 + S_\pm$.

When exposed to a femtosecond laser pulse, the time profile of the power density of the heat source is determined by the dynamics of the electron concentration in the CB and their energy density U:

$$S = \frac{\mathrm{d}U}{\mathrm{d}t} = \frac{9}{4}\left(\frac{\mathrm{d}\rho_c}{\mathrm{d}t}\right)\tilde{\Delta}. \tag{19}$$

Since the transfer by an electron of the energy accumulated in the focusing region in Eqn (7) is determined by the term describing recombination, expression (19) can be written as

$$S \approx \frac{9}{4}\left(\frac{\mathrm{d}\rho_c}{\mathrm{d}t}\right)_{\mathrm{rec}} \tilde{\Delta}. \qquad (20)$$

To study the temperature dynamics, differential equations (14)–(20) were solved using the finite element analysis (FEA) method, by analogy with Ref. [7].

3. Simulation results

To estimate the thermal effect of a femtosecond laser pulse, two problems are to be solved: to calculate the dynamics of the free electron concentration that determine the time profile of the heat source in the focusing region, and to calculate the temperature field $T(r,z)$ after the end of the laser pulse at different moments of time. To check the correctness of the solution of the corresponding problems, the initial parameters of the model were taken from previously published papers, and then the obtained dependences were compared. At the end of this section, the results of the calculation for the parameters of the laser pulse used for microsurgery of the embryo are presented.

3.1. Estimating the free electron concentration in the focusing region

To calculate the dynamics of the electron density ρ_c, Eqn (7), taking into account Eqns (1)–(5) and (8)–(10), was solved numerically by the Runge–Kutta method with an adaptive step. The results obtained (Figs 4–6) are compared with those of Ref. [20], in which an additional initiation channel was introduced into the model for the first time. In this work, the emission intensity I_0 of a laser pulse with a duration τ_L = 250 fs was 8.25×10^{12} W cm^{-2} (chosen as the average value corresponding to the experimentally measured intensity of the water breakdown threshold in the wavelength range of 330–1090 nm). Figure 4 shows the multiphoton ionisation rates η_{SFI} depending on the laser wavelength. Velocities decrease with increasing wavelength and number of photons required to overcome the band gap. The latter circumstance also explains the stepped profile of the curve. The obtained values (points in Fig. 4) demonstrate good agreement with the calculation results [20].

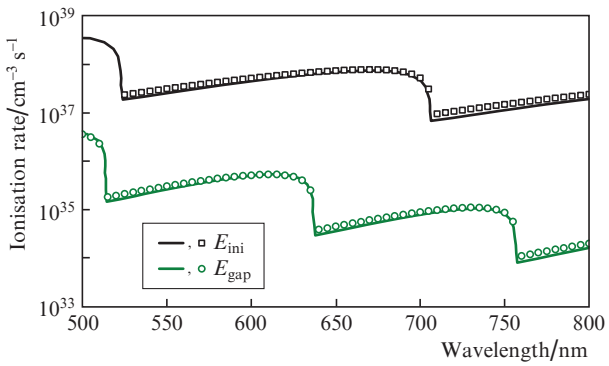

Figure 4. Dependences of the multiphoton ionisation rate for levels with energies E_{ini} and E_{gap} on the radiation wavelength. The calculations were carried out for the intensity $I_0 = 8.25 \times 10^{12}$ W cm^{-2}. Curves are data from Ref. [20]; dots are the results of the present work.

The contribution of each of the ionisation channels can be clearly seen in the dynamics of the free electron concentration (Fig. 5), calculated for the wavelength λ = 520 nm. The concentration in the initiation channel rapidly saturates and by the time point corresponding to the maximum intensity of the laser pulse (t = 0) already reaches its maximum value $\rho_{ini}^{max} = 10^{19}$ cm^{-3} [20]. Avalanche ionisation ($\rho_{AI} = \rho_c - \rho_{SFI}$) also begins to manifest itself closer to the intensity maximum (shown by the arrow), when a sufficient number of free electrons has been accumulated, and its contribution is $\rho_{AI}/\rho_{SFI} = 17$. In the general case, the contributions of multiphoton and avalanche ionisation depend on the laser pulse duration, band gap, and medium parameters that determine collisional processes. Any intermediate energy levels between the VB and the CB that exist in transparent dielectrics are also important. As noted earlier, the presence of an intermediate level with the energy E_{ini} in water is due to the special geometry of the molecular arrangement supported by weak hydrogen bonds. The latter can be destroyed by the electric field of CB electrons if they are accumulated in sufficient amount. The value $\rho_{ini}^{max} = 10^{19}$ cm^{-3}, coinciding with the capacitance χ_{trap} of the initiation channel, is an empirical parameter obtained in Ref. [20] by fitting the calculated value of the water breakdown threshold intensity $I_{th}(\lambda)$ to the experimental value in a wide wavelength range: λ = 330–1100 nm. In accordance with the observations of the authors of the present work, saturation occurs only for wavelengths $\lambda < 530$ nm. For longer wavelength radiation, the number of photons required for the transition of an electron to a level with energy E_{ini} changes from 3 to 4, and the value of $\rho_{ini}^{max}/\chi_{trap}$ becomes less than 60%.

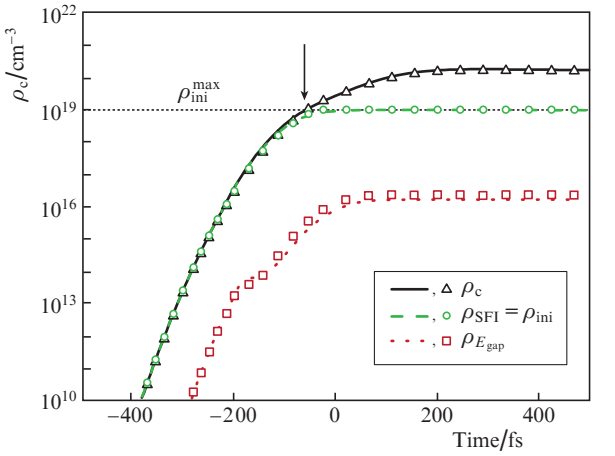

Figure 5. (Colour online) Electron density dynamics for a femtosecond pulse with duration τ_L = 250 fs and intensity $I_0 = 8.25 \times 10^{12}$ W cm^{-2} at a radiation wavelength λ = 520 nm. Curves are data from Ref. [20]; dots are the results of the present work.

Figure 6 illustrates estimates of the volume energy density U of electrons depending on the laser pulse intensity obtained in Ref. [21] for a pulse with duration τ_L = 250 fs at a radiation wavelength λ = 515 nm. The temperature increment was calculated using Eqn (13). The results of calculations performed in the present work (points in Fig. 6) demonstrate good agreement with the results obtained in Ref. [21] using SRE.

The dependence found makes it possible to estimate the temperature increment in the range of laser pulse intensities used for the embryo microsurgery. Thus, at a typical value of $I_0 = 2.5 \times 10^{12}$ W cm^{-2}, the expected temperature increase is a few degrees. At the same time, the value $I_0 = 7.5 \times 10^{12}$ W cm^{-2}, which is the limit value [43] for microsurgery at a wavelength $\lambda = 515$ nm due to the onset of cavitation bubbles formation, corresponds to a temperature increase $\Delta T \approx 100\,^{\circ}$C.

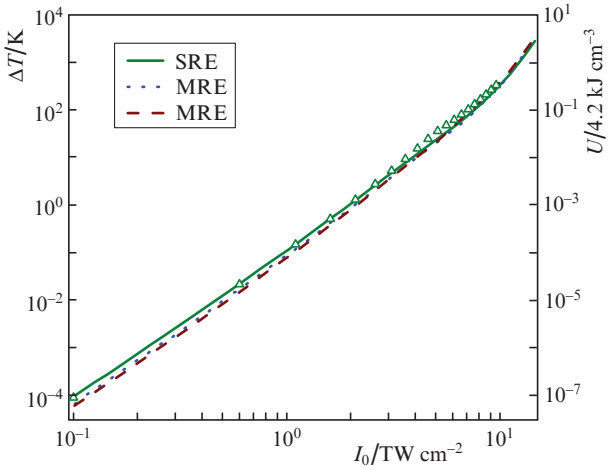

Figure 6. (Colour online) Dependences of the volume energy density U on the laser pulse intensity I_0 for a femtosecond pulse with duration $\tau_L = 250$ fs at a radiation wavelength $\lambda = 515$ nm. The temperature increment ΔT due to the energy contribution is determined by Eqn (13). Curves are data from Ref. [21] (two models for MRE were used); dots are the results of the present work.

3.2. Calculation of the temperature field after the end of the laser pulse action

To assess the dynamics of the spatial distribution of temperature, it is necessary to solve equations (15)–(17) given in Section 2.2. To estimate the accuracy of solving the heat transfer problem, we compared the results of the temperature assessment obtained in the present work with the results of Ref. [8] for a submillisecond pulse.

In laser dissectors used in clinical practice, the power of the radiation source is constant, and the pulse energy is controlled by changing its duration. Obviously, as the latter grows, the heating in the affected area will only increase; therefore, to estimate the minimum possible thermal effect on the embryo, the minimum achievable laser pulse duration $\tau_L = 0.6$ ms was used in the calculations. At the same time, it should be noted that in Ref. [8] there is a reference to protocols for microsurgery of human embryos for IVF clinics, in which the typical duration value is 0.8 ms.

The accuracy of solving the heat conduction problem was estimated by comparing the calculation results with the data obtained in Ref. [8] for $P = 245$ mW and $\tau_L = 0.6$ ms. The angle θ in Eqn (17) is determined by the numerical aperture of the microscope objective and, taking into account the refractive index of water for a collimated beam 1.3 mm in diameter entering the objective, amounts to 12.6°; the waist radius is $a = 2$ μm [8], and its length $b = 2a\cot\theta \approx 18$ μm (see Fig. 3).

The temperature dynamics in the waist plane $T(r, z = 0)$ is shown in Fig. 7. A series of curves is shown for various values of r, which make it possible to estimate the heating temperature at a given distance from the laser beam axis. Due to the small size of the heat source, there is a rapid cooling of the heated region after the end of the laser pulse – the temperature decreases by a factor of two from the maximum value of ~370 °C in a time of ~6 μs. One can note good agreement between the obtained temperature values (points in Fig. 7) and the results of the calculation (curves) performed in Ref. [8]. Discrepancies within 5% are due to the finite step Δr of the coordinate grid and the inaccuracy of the interpolation of values at the points specified by the section planes.

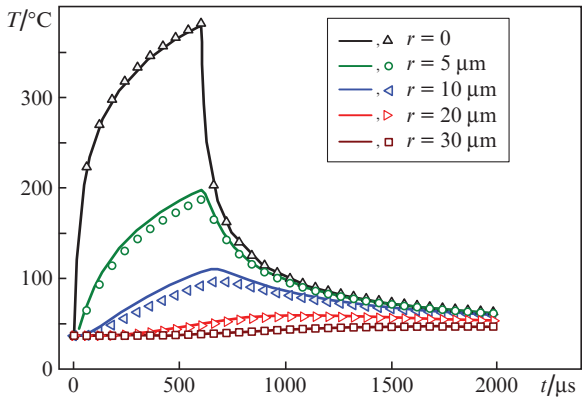

Figure 7. (Colour online) Temperature dynamics at different distances r from the laser beam axis in the waist plane. Curves are data from Ref. [8] ($\lambda = 1480$ nm, $\tau_L = 0.6$ ms, $P = 250$ mW, NA = 0.6); dots are the results of the present work.

3.3. Comparison of the thermal effects of femtosecond and millisecond pulses during the embryo microsurgery

Here are the results of modelling the interaction of a femtosecond pulse with an aqueous medium for the values of the radiation parameters used in the microsurgical procedure of assisted hatching or marking of the *zona pellucida* [10, 43]. The calculations were performed for the laser pulse at a wavelength $\lambda = 514$ nm having a Gaussian intensity time profile with a peak value $I_0 = 2.5 \times 10^{12}$ W cm^{-2}, FWHM duration $\tau_L = 280$ fs, focused by an Olympus UPLFLN 20$^{\times}$ microscope objective with a numerical aperture NA = 0.5 into a spot 1.9 μm in diameter at the 1/e level.

Figure 8 shows the time dependences of the laser pulse intensity $I(t)$ and the volume power density of the heat source $S(t)$ at the centre of the waist ($r = 0$, $z = 0$) of the laser beam. Note that for a laser pulse duration of several hundreds of femtoseconds, the value of $S(t)$ decreases by a factor of two on a time scale of the order of hundreds of picoseconds. Thus, the duration of the cooling stage under the action of laser USPs significantly exceeds the duration of the heating stage, which was qualitatively demonstrated by the authors of Ref. [48]. This circumstance suggests that there is a potential possibility of using picosecond laser sources in microsurgery.

Assuming the electron concentration in the CB at the end of the laser pulse to be proportional to $I^{k'}$, the spatial distribution can be written as

$$\rho_{\max}(r,z) = \rho_{\max}(I(0,0))\exp\left[-2k'\left(\frac{r^2}{a^2} + \frac{z^2}{b^2}\right)\right], \qquad (21)$$

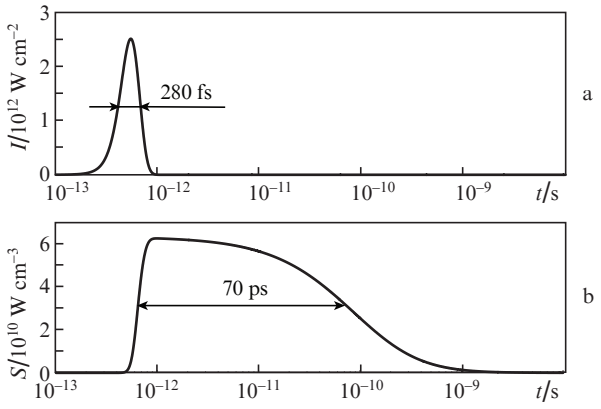

Figure 8. Time profiles of (a) the laser pulse intensity $I(t)$ and (b) the power volume density of the heat source $S(t)$ at the point with coordinates $r = 0$, $z = 0$ under the action of a femtosecond laser pulse.

where ρ_{max} is the maximum value of the electron concentration; and k' is the number of photons required for multiphoton ionisation. The radiation wavelength $\lambda = 514$ nm falls on the boundary of the transition from three-photon to four-photon absorption. The calculation of the dependence of the maximum concentration values on the laser pulse intensity $\rho_{max}(I)$ at the point (0, 0) showed (points in Fig. 9) that the best agreement with Eqn (21) is achieved at $k' = 3–4$. The data obtained allowed estimating the temporal and spatial profiles of the heat source power density to solve the heat transfer problem formulated in Section 2.2.2.

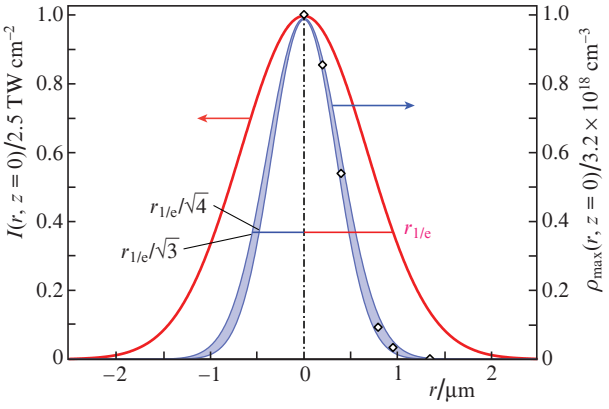

Figure 9. (Colour online) Spatial distributions of the intensity $I(r, z=0)$ and the maximum electron concentration $\rho_{max}(r, z=0)$ at the focus of the laser pulse.

To demonstrate significant differences, Fig. 10 shows the spatial distributions of maximum temperatures in the focusing region, achieved as a result of exposure to millisecond (Fig. 10a) and femtosecond (Fig. 10b) pulses. In the first case, the distribution $T(r, z)$ was obtained at the time $t = 0.6$ ms, i.e., at the end of the laser pulse. In the second case, the maximum temperature is reached at times $t \approx 10$ ns (Fig. 10c) after the end of the pulse. The white lines in Figs 10a and 10b show the geometry of the laser beam. Isotherms are plotted in 20 °C increments.

For a millisecond pulse, the calculation was performed for the values of the parameters used in Ref. [8] for microsurgery

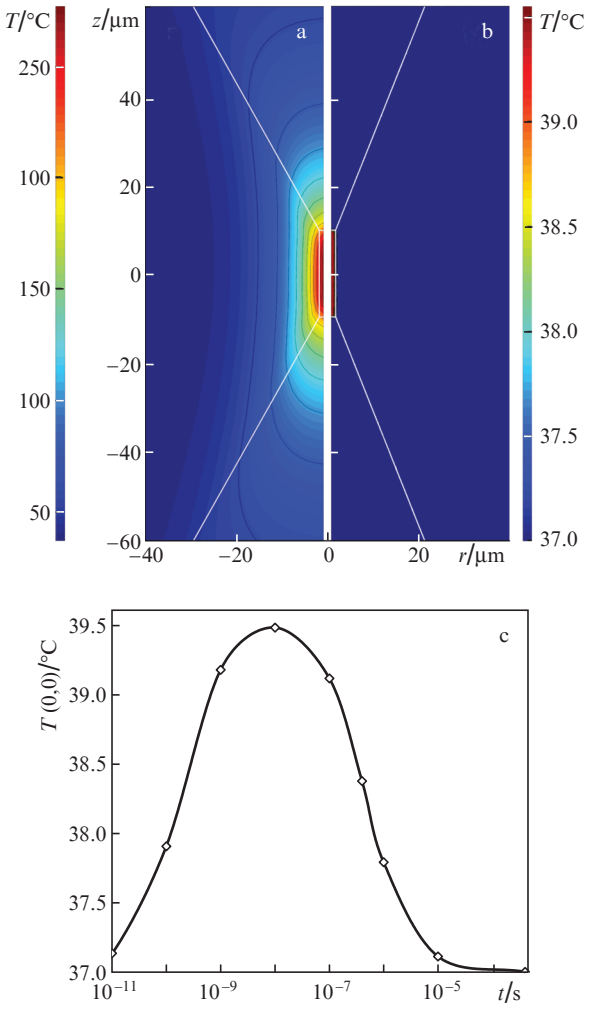

Figure 10. (Colour online) Results of the FEA calculation of maximum temperatures as a result of the absorption of (a) millisecond and (b) femtosecond laser pulses in an aqueous medium, as well as (c) the temperature dynamics in the centre of the spot $T(0, 0)$ under femtosecond exposure. Initial medium temperature $T_0 = 37$ °C, $\lambda = 1480$ nm, $\tau_L = 0.6$ ms, $P = 180$ mW, temperature at the centre 270 °C (a) and $\lambda = 514$ nm, $\tau_L = 280$ fs, $I_0 = 2.5 \times 10^{12}$ W cm^{-2}, temperature in the centre 39.5 °C (b). The isotherm lines are plotted with a step of 20 °C. The white lines show the geometry of the laser beam.

of the *zona pellucida* of mouse, hamster, and cow embryos, which provide the minimum energy input, namely, $P = 180$ mW, $\tau_L = 0.6$ ms. As a result of pulse absorption, a region of superheated water is formed in the form of a cylinder with a diameter of ~20 μm and a height of ~100 μm. In the case of a femtosecond pulse, the change in temperature does not exceed 2.5 °C. The calculation results demonstrate a significantly better temperature localisation for femtosecond pulses, which is due to the geometry of the heat source described by expressions (19)–(21).

The dynamics of the spatial distribution of temperature is shown in Fig. 11 for millisecond and femtosecond laser pulses. With a millisecond exposure, the temperature reaches more than 80 °C in the vicinity with a radius of 10 μm from the centre of the beam and 50 °C in the vicinity with a radius of 20 μm. This circumstance imposes significant restrictions on the performance of microsurgical procedures (drilling, thinning, 'opening' the *zona pellucida*) due to the high risks of thermal damage to the embryonic cells adjacent to the *zona*

pellucida from the inside. When a femtosecond pulse is absorbed, the size of the thermal impact area is comparable to the diameter of the laser radiation focusing spot, which creates the prerequisites for safe microsurgical procedures with the *zona pellucida* even when the embryonic cells are directly adjacent to the membrane in the impact area.

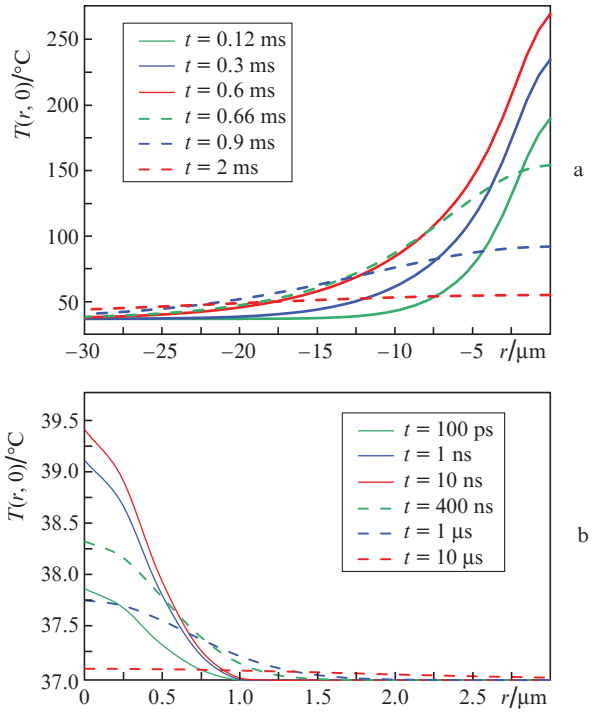

Figure 11. (Colour online) Radial temperature profiles $T(r, z=0)$ at different moments of time for (a) millisecond and (b) femtosecond pulses. Solid curves are the heating stage; dashed curves are the cooling stage.

4. Conclusions

The aim of this study was to evaluate the thermal impact of femtosecond laser pulses during microsurgical procedures within the ART. We used the model of absorption of femtosecond pulses in an aquatic environment, which was described in detail by a group of authors in a series of papers of 2003–2019 [18–21], to estimate the dynamics of electrons in the focusing region. The reliability of the simulation results was confirmed earlier by the authors of the mentioned papers in experimental studies of water breakdown by laser radiation pulses [49].

The model equations were solved numerically in the MATLAB environment. The spatial and temporal characteristics of the heat source were obtained by solving the heat transfer problem to estimate the spatial distribution of temperature after the end of the laser pulse. The parameters of femtosecond laser pulses used for the successful implementation of such microsurgical procedures as dissection and microengraving of the *zona pellucida* ($\lambda = 514$ nm, $\tau_L = 280$ fs, $I_0 = 2.5 \times 10^{12}$ W cm^{-2}) were taken as input parameters of the model. As a result, the spatial distribution of temperature in the focusing region was found, and the dynamics of the temperature field after the end of the femtosecond pulse action was studied. The obtained results are compared with the data for the parameters of laser pulses used in millisecond laser dissectors in IVF clinics.

It is shown that the maximum temperature reached in the centre of the focusing region under the action of a femtosecond laser pulse and at the parameters we specified is 39.5 °C, which is much lower than the temperature reaching 350 °C under the action of a millisecond laser pulse. In addition, in the case of femtosecond pulses, the processes of nonlinear (multiphoton) absorption make it possible to localise the impact area to the limit. Thus, the radius of the generated heat source is approximately two times smaller than the waist radius of the laser beam, which opens up the possibility of performing microsurgical procedures with subdiffraction accuracy.

It is also worth noting that the duration of the existence of a heat source created in the focusing region is several orders of magnitude longer than the duration of the laser pulse itself. This circumstance creates prerequisites for the use of picosecond laser sources for performing microsurgical procedures. However, the answer to the question of its expediency requires additional studies and is beyond the scope of this work.

Acknowledgements. The work was supported by the Ministry of Science and Higher Education of the Russian Federation (State Assignment No. 075-01056-22-00).

References

1. Tirlapur U.K., König K. *Nature*, **418**, 290 (2002).
2. Ferrando-May E., Tomas M., Blumhardt P., Stöckl M., Fuchs M., Leitenstorfer A. *Front. Genet.*, **4**, 135 (2013).
3. Chung S.H., Mazur E. *J. Biophotonics*, **2**, 557 (2009).
4. Friedman N.J., Palanker D.V., Schuele G., Andersen D., Marcellino G., Seibel B.S., Batlle J., Feliz R., Talamo J.H., Blumenkranz M.S., Culbertson W.W. *J. Cataract Refract. Surg.*, **37**, 1189 (2011).
5. Hoy C.L., Ferhanoglu O., Yildirim M., Ki Hyun Kim, Karajanagi S.S., Chan K.M.C., Kobler J.B., Zeitels S.M., Ben-Yakar A. *IEEE J. Sel. Top. Quantum Electron.*, **20**, 242 (2014).
6. Ratkay-Traub I., Ferincz I.E., Juhasz T., Kurtz R.M., Krueger R.R. *J. Refract. Surg.*, **19**, 94 (2003).
7. Douglas-Hamilton D.H., Conia J. *J. Biomed. Opt.*, **6**, 205 (2001).
8. Tadir Y., Douglas-Hamilton D.H. *Methods Cell Biol.*, **82**, 409 (2007).
9. Chatzimeletiou K., Morrison E.E., Panagiotidis Y., Prapas N., Prapas Y., Rutherford A.J., Grudzinskas G., Handyside A.H. *Reprod. Biomed. Online*, **11**, 697 (2005).
10. Ilina I.V., Khramova Y.V., Filatov M.A., Sitnikov D.S. *J. Assist. Reprod. Genet.*, **36**, 1251 (2019).
11. Ilina I.V., Khramova Y.V., Ivanova A.D., Filatov M.A., Silaeva Y.Y., Deykin A.V., Sitnikov D.S. *J. Assist. Reprod. Genet.*, **38**, 517 (2021).
12. Mao S.S., Quéré F., Guizard S., Mao X., Russo R.E., Petite G., Martin P. *Appl. Phys. A: Mater. Sci. Process.*, **79**, 1695 (2004).
13. Rethfeld B. *Phys. Rev. Lett.*, **92**, 187401 (2004).
14. Gulley J.R. *Proc. SPIE*, **8190**, 819022 (2011).
15. Geints Yu.E., Golik S.S., Zemlyanov A.A., Kabanov A.M., Petrov A.V. *Quantum Electron.*, **46**, 133 (2016) [*Kvantovaya Elektron.*, **46**, 133 (2016)].
16. Jeong B., Lee B., Kim J.H., Choi J.A., Yang J., Sall E.G., Kim J.W., Heo D., Jang J., Kim G.H., Yashin V.E. *Quantum Electron.*, **50**, 201 (2020) [*Kvantovaya Elektron.*, **50**, 201 (2020)].
17. Guo B., Sun J., Hua Y., Zhan N., Jia J., Chu K. *Nanomanufacturing Metrol.*, **3**, 26 (2020).
18. Vogel A., Venugopalan V. *Chem. Rev.*, **103**, 577 (2003).
19. Vogel A., Noack J., Hüttman G., Paltauf G. *Appl. Phys. B*, **81**, 1015 (2005).
20. Linz N., Freidank S., Liang X.X., Vogel A. *Phys. Rev. B*, **94**, 1 (2016).
21. Liang X.-X., Zhang Z., Vogel A. *Opt. Express*, **27**, 4672 (2019).
22. Docchio F., Sacchi C., Marshall J. *Lasers Ophthalmol.*, **1**, 83 (1986).

23. Williams F., Varma S.P., Hillenius S. *J. Chem. Phys*., **64**, 1549 (1976).
24. Elles C.G., Jailaubekov A.E., Crowell R.A., Bradforth S.E. *J. Chem. Phys*., **125**, 044515 (2006).
25. Sander M.U., Gudiksen M.S., Luther K., Troe J. *Chem. Phys*., **258**, 257 (2000).
26. Bartels D.M., Crowell R.A. *J. Phys. Chem. A*, **104**, 3349 (2000).
27. Linz N., Freidank S., Liang X.-X., Vogelmann H., Trickl T., Vogel A. *Phys. Rev. B*, **91**, 134114 (2015).
28. Son D.H., Kambhampati P., Kee T.W., Barbara P.F. *J. Phys. Chem. A*, **105**, 8269 (2001).
29. Keldysh L.V. *Sov. Phys. JETP*, **20**, 1307 (1965) [*Zh. Eksp. Teor. Fiz*., **47**, 1945 (1965)].
30. Kennedy P.K. *IEEE J. Quantum Electron*., **31**, 2241 (1995).
31. Christensen B.H., Balling P. *Phys. Rev. B*, **79**, 155424 (2009).
32. Kaiser A., Rethfeld B. *Phys. Rev. B: Condens. Matter Mater. Phys*., **61**, 11437 (2000).
33. Docchio F. *Europhys. Lett*., **6**, 407 (1988).
34. Sarpe-Tudoran C., Assion A., Wollenhaupt M., Winter M., Baumert T., Assion A., Wollenhaupt M., Winter M., Baumert T. *Appl. Phys. Lett*., **88**, 261109 (2006).
35. Davidson L.M., Liu Y., Griffiths T., Jones C., Coward K. *Reprod. Biomed. Online*, **38**, 725 (2019).
36. Ilina I.V., Khramova Y.V., Filatov M.A., Semenova M.L., Sitnikov D.S. *High Temp*., **54**, 46 (2016).
37. Ilina I.V., Khramova Y.V., Filatov M.A., Semenova M.L., Sitnikov D.S. *High Temp*., **53**, 804 (2015).
38. Ilina I.V., Rakityanskiy M.M., Sitnikov D.S., Ovchinnikov A.V., Agranat M.B., Khramova Y.V., Semenova M.L. *AIP Conf. Proc*., **1464**, 560 (2012).
39. Krivokharchenko A., Karmenyan A., Sarkisov O., Bader M., Chiou A., Shakhbazyan A. *PLoS One*, **7**, e50029 (2012).
40. Osychenko A.A., Zalesskii A.D., Krivoharchenko A.S., Shakhbazyan A.K., Ryabova A.V., Nadtochenko V.A. *Quantum Electron*., **45**, 498 (2015) [*Kvantovaya Elektron*., **45**, 498 (2015)].
41. Ilina I.V., Filatov M.A., Khramova Y.V., Sitnikov D.S. *Proc. 2020 Int. Conf. Laser Optics (ICLO)* (St. Petersburg, IEEE, 2020).
42. Ilina I.V., Khramova Y.V., Filatov M.A., Sitnikov D.S. *Proc. SPIE*, **11079**, 110798 (2019).
43. Ilina I.V., Khramova Y.V., Filatov M.A., Sitnikov D.S. *Biomed. Opt. Express*, **10**, 2985 (2019).
44. Hogan B., Beddington R., Costantini F., Lacy E. *Manipulating the Mouse Embryo: A Laboratory Manual* (New York: Cold Spring Harbor Lab., 2014).
45. Sitnikov D.S., Ovchinnikov A.V., Ilina I.V., Chefonov O.V., Agranat M.B. *High Temp*., **52**, 803 (2014).
46. Ramires M.L.V., Nieto de Castro C.A., Nagasaka Y., Nagashima A., Assael M.J., Wakeham W.A. *J. Phys. Chem. Ref. Data*, **24**, 1377 (1995).
47. Hale G.M., Querry M.R. *Appl. Opt*., **12**, 555 (1973).
48. Veiko V.P., Shakhno E.A., Yakovlev E.B. *Quantum Electron*., **44**, 322 (2014) [*Kvantovaya Elektron*., **44**, 322 (2014)].
49. Vogel A., Linz N., Freidank S., Paltauf G. *Phys. Rev. Lett*., **100**, 038102 (2008).